Shear Alfvén waves in a magnetic beach and the roles of electron and ion damping

S. Vincena,[a] W. Gekelman, and J. Maggs
Department of Physics and Astronomy, University of California, Los Angeles, California 90095

(Received 29 January 2001; accepted 11 June 2001)

Experiments are performed in the Large Plasma Device (LaPD) [Gekelman *et al.*, Rev. Sci. Instrum. **62**, 2875 (1991)] at the University of California, Los Angeles to study the propagation of the shear Alfvén wave in a parallel gradient of the background magnetic field. The waves are excited by modulating a field-aligned electron current drawn to a disk antenna with a radius on the order of the electron skin-depth, $\delta = c/\omega_{pe}$. The resulting shear waves have a nonzero parallel electric field and propagate both parallel and perpendicular to the background magnetic field. In this experiment, the wave is launched in a region where its frequency, ω equals one-half the local ion-cyclotron frequency, ω_{ci} and the local Alfvén speed, v_A, is approximately equal to the electron thermal speed, $\overline{v_e}$. The wave propagates along a slowly decreasing background field to where $\omega = \omega_{ci}$ and $v_A \approx \overline{v_e}/2$. The wave thus propagates from a region where Landau damping is significant to where ion-cyclotron damping dominates. Detailed two dimensional measurements of the wave magnetic field morphology are presented. The measured wavelength decreases in accord with WKB solutions of a modified wave equation. Wave damping is also observed and dissipation by both ions and electrons is required in the WKB model to fit the data. Suppression of the damping via electrons in the model results in a predicted wave magnetic field amplitude twenty times larger at the ion-cyclotron resonance point than observed. © *2001 American Institute of Physics.*
[DOI: 10.1063/1.1389092]

I. INTRODUCTION

The shear Alfvén wave is an electromagnetic wave in a magnetized plasma which propagates at frequencies below the ion-cyclotron frequency. This type of wave may be found everywhere from the Sun, the magnetosphere of the Earth (and other planets) to fusion research plasmas. In the myriad environments where the shear Alfvén wave is found, many contain spatial nonuniformities in a variety of plasma parameters. The study of waves in the presence of nonuniformities has added greatly to our understanding of basic plasma physics and, as plasmas in the laboratory and in space are probed with ever-increasing spatial and temporal resolution, new mysteries arise to stimulate further research. This is a study of the propagation from a localized source of an axisymmetric ($m=0$ mode) shear Alfvén wave in a laboratory plasma in the presence of a parallel gradient in the background magnetic field. Alfvén waves produced by small-scale current fluctuations appear to be a ubiquitous and important phenomenon for understanding the complex dynamics of the Earth's ionosphere. Although the studies of Alfvén waves from small sources are still relatively recent, it is the scarcity of laboratory work aimed at understanding how these waves behave in the presence of spatial nonuniformities which motivates the present experiments.

Some of the earliest work on Alfvén waves in nonuniform magnetic fields was performed by researchers[1,2] studying the excitation of radial eigenmodes of a cylindrical plasma which then propagated axially into a region of decreasing magnetic field to the point where the wave frequency matched the local ion-cyclotron frequency—the so-called ''magnetic beach.'' Much later, Amagishi *et al.*[3] observed the mode conversion of an axisymmetric global compressional Alfvén mode to the shear wave along an increasing parallel magnetic field. The launching mechanism for the compressional wave was a Helmholtz-like coil with a diameter equal to the plasma diameter. The results were consistent with the fluid-theory predictions of Woods[4] for oscillations in a bounded, cylindrical plasma.

The development of mirror machines for fusion research provided a convenient arena to study the propagation of Alfvén waves in parallel magnetic field gradients. In particular, research in the heating of plasmas to attain fusion temperatures prompted the study of Alfvén waves near the ion-cyclotron resonance—termed ICRF heating. Naturally, since these experiments were intended to heat the bulk plasma, the focus was on global eigenmodes and not on controlled wave excitation by localized sources. For example, ICRF heating was studied in the THM-2 mirror machine[5] using a Stix-type[1] coil exciter, and in the Phaedrus-B tandem mirror[6] using a rotating field antenna[7,8] which selectively excited a global, $m=-1$ eigenmode of the shear Alfvén wave and was found to efficiently transfer energy to the ions. Additionally, the loss of wave energy to the electrons was pointed out in a theoretical study of Alfvén wave heating in open confinement systems by Zvonkov and Timofeev;[9] there, the authors considered the mode conversion of compressional to shear waves at the Alfvén resonance layer.

[a]Electronic mail: vincena@physics.ucla.edu

Few studies to date have been done on the propagation of Alfvén waves from small, localized sources. Spontaneous fluctuations were observed by Zweben *et al.*[10] in the Macrotor tokamak. An investigation of localized shear Alfvén waves including the effects of parallel wave electric fields were made by Borg *et al.*[11] in the TORTUS tokamak[12] using small, magnetic dipole antennas. The wave magnetic fields from the localized source were observed to spread across the background field lines, in contrast with the ideal magnetohydrodynamic picture. The electron–neutral collision rate in this experiment was high enough that the radial propagation was dominated by resistive spreading of the wave fields.

In a pair of theoretical papers beginning in 1994, Morales *et al.*[13,14] studied the radiated azimuthal shear Alfvén wave magnetic field from small perpendicular scale sources in two parameter regimes: $v_A \gg \overline{v_e}$ and $v_A \ll \overline{v_e}$. Here, v_A is the Alfvén speed ($v_A = B/\sqrt{4\pi n_i m_i}$, B is the background field strength, n_i and m_i are the ion density and mass, respectively) and $\overline{v_e} \equiv \sqrt{2T_e/m_e}$ is the average electron thermal speed, with T_e the electron temperature and m_e the electron mass. The first case ($v_A \gg \overline{v_e}$) is relevant to the conditions near the edge and limiter regions of tokamak plasmas and in the Earth's ionosphere. In this limit, the shear wave is termed the ''inertial Alfvén wave.'' The propagation of the inertial wave from a source having transverse scale on the order of the electron skin-depth (c/ω_{pe}) was found to be governed by a collisionless divergence determined by propagation cones that emanate from the edges of the exciter. In the second case ($v_A \ll \overline{v_e}$) the shear wave is called the ''kinetic Alfvén wave,'' and is more relevant to the physics of the Earth's magnetotail and to the interior regions of tokamak plasmas. The radiation pattern of the kinetic wave from small sources was also found to spread radially, but in a more complicated fashion than the inertial wave. In the magnetosphere, the transition region between these two regimes (where $v_A = \overline{v_e}$ and Landau damping must be considered) is currently not well understood by the space plasma community, but may be important in understanding the behavior of Alfvén resonances on auroral field lines.[15]

Concurrent with the publication of the theoretical investigations by Morales *et al.*, a series of experimental work[16–19] served to verify and expand on the understanding of the Alfvén wave in both of these regimes. In 1994, Gekelman *et al.*[16] used a skin-depth-scale disk antenna (of the same type used in this experiment) to excite the inertial Alfvén wave and verified the predicted radiation pattern[13] including the spreading of wave magnetic field energy perpendicular to the background field. In 1997, Gekelman *et al.*[17] made similar observations with the kinetic Alfvén wave. Leneman[18] studied both the inertial and kinetic waves (using a sandwiched composite of two disk antennas) for a wide range of plasma conditions including the effects of collisions.

Low-frequency electromagnetic wave emissions have long been associated with auroral phenomena. In 1972, the polar-orbiting satellite, Injun 5 detected monochromatic ELF (extremely low frequency) radio bursts at frequencies below the proton gyrofrequency; these bursts were associated with low-energy auroral electron precipitation.[20] Statistical measurements of the data from the S3-3 satellite in 1984,[21] and the ISIS-1 and ISIS-2 satellites in 1987[22] showed that these emissions were consistent with electromagnetic ion-cyclotron waves—which is simply the shear Alfvén wave at frequencies near the ion-cyclotron frequency. The observation of these low-frequency waves and their correlation with electron precipitation was subsequently made by the Viking satellite[23] during nightside auroral field line crossings.

In observations from the FREJA satellite reported by Louarn *et al.* in 1994,[24] strong low-frequency electromagnetic spikes were encountered with $\Delta E/\Delta B$ on the order of v_A/c. The authors attributed the spike-like nature of the signals to the satellite passing through solitary structures with scale sizes on the order of the electron skin-depth. These phenomena were dubbed SKAWS (solitary kinetic Alfvén waves). The ''kinetic'' portion of this nomenclature is unfortunate, since it was intended to merely distinguish it from the ideal MHD limit, whereas the term ''kinetic Alfvén wave'' is properly applied to the shear Alfvén wave in the limit $v_A \ll \overline{v_e}$. In the low altitude auroral ionosphere, the opposite is generally true: $v_A \gg \overline{v_e}$, so that SKAWS are actually manifestations of the inertial Alfvén wave. Later investigations by Volwerk *et al.* in 1996[25] provided a more detailed examination of SKAWS. It was determined that the SKAWS were tubular current structures of skin-depth scale with $\Delta B_\parallel/\Delta B \approx 10\%$, and they were situated at the edge of large-scale shear regions in the current.

More recently, shear waves have been observed by the Fast Auroral SnapshoT (FAST) satellite[26] in regions of field-aligned electron fluxes and are believed to be responsible for both modulating these electron fluxes[27] and accelerating ions perpendicular to the background magnetic field to energies of several keV.[28] A comprehensive review of laboratory experiments on Alfvén waves and their relationship to space observations may be found in the recent publication by Gekelman.[29]

The remainder of the manuscript is organized as follows: in Sec. II a review is presented of the theoretical aspects of the shear Alfvén wave relevant to these experiments. In Sec. III we describe the experimental device, antenna and data acquisition. The experimental findings are presented in Sec. IV followed by concluding remarks in Sec. V.

II. REVIEW OF SHEAR ALFVÉN WAVES FROM SMALL SOURCES

The shear Alfvén wave radiation from small disk antennas (as used in the present experiments) has been previously studied both theoretically and experimentally. The source of the Alfvén wave in either case is a harmonically modulated electron current filament with transverse size on the order of the electron collisionless skin-depth or the ion sound gyroradius. Morales *et al.* have derived an integral expression for the spatial dependence of the radiated magnetic field in an infinite, uniform plasma,[13,14]

$$\mathbf{B} = \left[\frac{4\pi}{c} \int_0^\infty \tilde{J}_A J_1(k_\perp r) e^{ik_\parallel z} dk_\perp \right] \hat{\theta}, \tag{1}$$

where J_1 is the first-order Bessel function, and $\tilde{J}_A$ is the Hankel transform of the field-aligned current density drawn to the antenna at $z=0$ and $\hat{\theta}$ is the azimuthal unit vector. In contrast to the standard MHD description, Alfvén waves radiated from small cross-field sources have a parallel electric field and propagate perpendicular as well as parallel to the background magnetic field.

Experiments by Gekelman *et al.*[16,17] have verified the predicted spatial form of the radiation patterns. The waves are observed to satisfy the cold plasma shear Alfvén wave dispersion relation. The waves are cylindrically symmetric, as expected from the symmetry of the exciter. The wave magnetic field is confirmed to be primarily in the azimuthal direction and the field has zero magnitude on axis with the exciter. The field amplitude increases with radial distance from the exciter, reaches a peak value and then decays. The pattern is analogous to the magnetostatic picture of the field from a current carrying wire of finite radius. The radial peak of the field magnitude moves outward with an increasing axial distance from the antenna since the wave propagates perpendicular as well as parallel to the magnetic field. The angle of propagation with respect to the background field is small (a few degrees) since the perpendicular group velocity of the wave is much smaller than the parallel group velocity.

These previous experiments have focused on the shear Alfvén waves radiated by small sources in various limiting cases: $\omega \ll \omega_{ci}$, $v_A \gg \overline{v_e}$ and $v_A \ll \overline{v_e}$. In the present experiment, we study this same short perpendicular wavelength radiation but in regimes where wave particle damping is important: $\omega \approx \omega_{ci}$ (ion-cyclotron damping) and $v_A \approx \overline{v_e}$ (electron Landau damping). To study the shear wave under these conditions, we must use a dispersion relation which incorporates these loss mechanisms. In an infinite, uniform plasma, the general dispersion relation for azimuthally symmetric shear Alfvén wave propagation ($m=0$ cylindrical modes, or equivalently, $k_y=0$ in Cartesian coordinates) may be written as

$$n_\perp^2 n_\parallel^2 = (n_\parallel^2 - \epsilon_{xx})(n_\perp^2 - \epsilon_\parallel) + \epsilon_{xy}^2 (n_\perp^2 - \epsilon_\parallel)/(n^2 - \epsilon_{xx}). \quad (2)$$

For the elements of the dielectric tensor, we use the appropriate terms provided by Stix:[30]

$$\epsilon_{xx} = \frac{1}{2}\left(\frac{\omega_{pi}}{\omega}\right)^2 \left[\frac{\omega}{k_\parallel \overline{v_i}} Z\left(\frac{\omega-\omega_{ci}}{k_\parallel \overline{v_i}}\right) - \frac{\omega}{\omega+\omega_{ci}}\right]$$

and

$$\epsilon_{xy} = \frac{i}{2}\left(\frac{\omega_{pi}}{\omega}\right)^2 \left[\frac{\omega}{k_\parallel \overline{v_i}} Z\left(\frac{\omega-\omega_{ci}}{k_\parallel \overline{v_i}}\right) + \frac{\omega}{\omega+\omega_{ci}} - 2\frac{\omega}{\omega_{ci}}\right],$$

where $\overline{v_i}$ is the average ion thermal speed ($\overline{v_i^2} = 2T_i/m_i$). The function Z is the plasma dispersion function[31] which is retained to include the effects of ion-cyclotron damping when $\omega \approx \omega_{ci}$. Numerical values for Z are obtained using an algorithm developed for computation of the complex error function.[32] The first two bracketed terms in ϵ_{xy} are due to the ion response and the final term: $2\omega/\omega_{ci}$ is a contribution from the electrons. Both ϵ_{xx} and ϵ_{xy} include simplifications based on the assumption that $(k_\perp \overline{v_i}/\omega_{ci})^2/2 \ll 1$.

The usual parallel element (which is dominated by the electron response) is given by

$$\epsilon_\parallel = -\left(\frac{\omega_{pe}}{\omega}\right)^2 \zeta_e^2 Z'(\zeta_e),$$

where ζ_e is the ratio of the parallel wave phase speed to the average electron thermal speed ($\zeta_e \equiv \omega/k_\parallel \overline{v_e}$) and Z' is the derivative of the plasma dispersion function with respect to its argument.

In order to estimate the effects of collisions (which are primarily due to electron–ion Coulomb interactions under our experimental conditions), $\epsilon_\parallel$ is modified by including a Krook collision operator in the linearized Vlasov equation resulting in

$$\epsilon_\parallel = -\left(\frac{\omega_{pe}}{\omega}\right)^2 \zeta_e \eta_e Z'(\eta_e),$$

where the derivative of Z is now with respect to the new argument: $\eta_e \equiv \zeta_e(1+i\Gamma)$; Γ is the ratio of the collision frequency to the angular wave frequency: ν_{ei}/ω, and ν_{ei} is the electron–ion Coulomb collision frequency as given by Koch and Horton:[33]

$$\nu_{ei} = 2\pi n e^4 \ln\Lambda / m_e^2 \overline{v_e}^3,$$

with the Coulomb logarithm $\ln\Lambda$ having the approximate value of 11 in these experiments.

III. EXPERIMENTAL ARRANGEMENT

A. Experimental device

These experiments are performed in the Large Plasma Device (LaPD) at the University of California, Los Angeles (UCLA).[34] The device is a stainless steel cylindrical vacuum chamber which is 10 m in length and 1 m in diameter. The chamber is surrounded by 68 pancake electromagnets fed by seven separate power supplies—this allows for a variety of axial field configurations. The plasma is produced by means of a pulsed electron discharge (between a heated nickel sheet cathode and a planar copper mesh anode) into a background of neutral gas (helium in these experiments) at pressures of approximately 1×10^{-4} Torr. The cathode is coated with a thin ($\approx 5\times10^{-3}$cm) circular layer of barium-oxide which reduces the work function of the electrons within the nickel.

The cathode and anode are located at one end of the device and are separated by a distance of 94 cm. The plasma which extends beyond this cathode–anode source region becomes nearly fully ionized within several milliseconds after which the main discharge plasma can be made to last up to 10's of milliseconds. Outside the source region, the typical helium plasma density is approximately 2×10^{12} cm^{-3} (as measured with a 56 GHz swept homodyne interferometer[35]), the electron temperature is 6–8 eV (measured with Langmuir probes), and the ion temperature is 1 ± 0.5 eV (measured using a Fabry–Pérot interferometer).

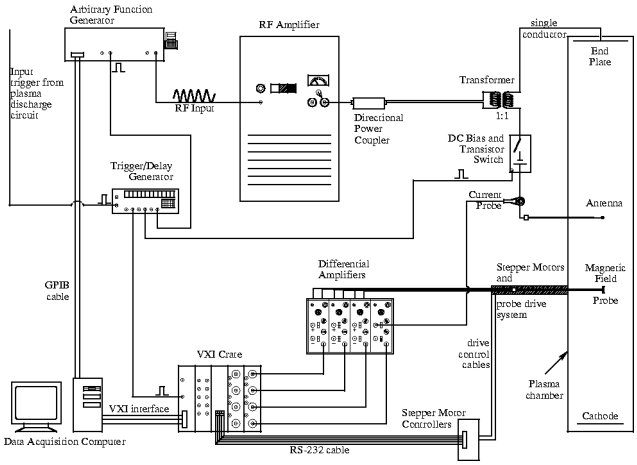

FIG. 1. Schematic for the wave launching antenna, magnetic field probe and data acquisition system. All unlabeled cables are 50 Ω coaxial cables.

B. Wave launching and detection

The wave launching antenna is the same design as used in previous shear Alfvén wave experiments[16,17,19] and is simply a 1 cm diameter circular copper mesh of 50% optical transparency. The antenna is inserted into the plasma and the normal to the plane of the antenna is aligned with the background magnetic field. A positive bias pulse is applied to the antenna for several hundred microseconds during the plasma discharge; the antenna bias is with respect to a floating copper end plate which terminates the plasma column. A typical experimental setup is shown schematically in Fig. 1. The bias voltages used are between 15 and 25 Volts which results in currents of approximately one-tenth of the electron saturation value and depletions of field-aligned density of approximately 5%. The waves are launched by modulating this effectively steady state current (through an isolation transformer) with a phase-locked tone burst from a rf amplifier at frequencies below the ion-cyclotron frequency. The vector components of the radiated wave magnetic fields are detected using a probe comprising three sets of oppositely wound induction coils. The component signals are first differentially amplified to remove common mode pickup and then digitized with a computer controlled data acquisition system.[36] This system is also used to automatically move probes in multiple dimensions, control the signal source wave form (frequency, duration, etc.) and vary the experimental timing.

IV. EXPERIMENTAL RESULTS

A. Uniform plasma dispersion relation

The ability of the disk exciter to launch an azimuthally symmetric ($m=0$) shear Alfvén wave in the LaPD has been established in previous experiments[16,17] for frequencies below $\omega=0.8\omega_{ci}$. This was accomplished through measurements of the azimuthal magnetic field, B_θ in an axially uniform background magnetic field. What has not yet been established is that this same antenna also radiates a definite axial wave magnetic field (B_z) at frequencies below the ion-cyclotron frequency which arises from the relative slippage in the $E\times B$ drifts of the ions and electrons as part of the shear wave collective particle motion. Before conducting the wave experiments in a nonuniform field, we find it prudent to begin by comparing measurement to theory of the parallel wave phase speed in a uniform plasma over the range of scaled frequencies ($\bar{\omega}\equiv\omega/\omega_{ci}$) which will be present in the nonuniform experiment.

The wave dispersion measurements are performed by determining the phase delay of the z-component of the wave magnetic field between four axial locations, all of which are on the same field line as the antenna. To accomplish this, a disk antenna of radius, $r_s=0.5$ cm ($\approx c/\omega_{pe}$) is first placed at the radial center ($r=0$) of the 35 cm plasma column at an axial location defined to be $z=0$ as shown in Fig. 2. The diameter of the plasma column is determined by taking the full-width at half the maximum value of a density profile. A three-axis magnetic field probe (of transverse size less than r_s) is also placed at the point $r=0$, but displaced axially by a distance of $z_1=94$ cm. The point, $r=0$, is determined by centering the probe at the point of the minimum received signal from the B_x and B_y probe coils while a 200 kHz (chosen arbitrarily) Alfvén wave is launched from the antenna. The perpendicular components of the wave field are measured to be zero at $r=0$ while B_z is at or near its maximum value. By measuring B_z at this point, it is assured that the probe will be located on the field line connecting to the center of the antenna and therefore all axial measurement locations will be field-aligned; additionally, at $r=0$ there is no need to account for measurement errors in the parallel phase speed due to radial propagation since the radial phase shifts enter as $e^{ik_\perp r}$. With the probe thus aligned, a 20-cycle, phase-locked tone burst is launched from the antenna at a frequency of $\bar{\omega}=0.5$, and the resultant B_z time series at z_1 is digitized and stored. The measurements are repeated until an ensemble average over 40 plasma discharges is recorded. The wave frequency is then increased and the process re-

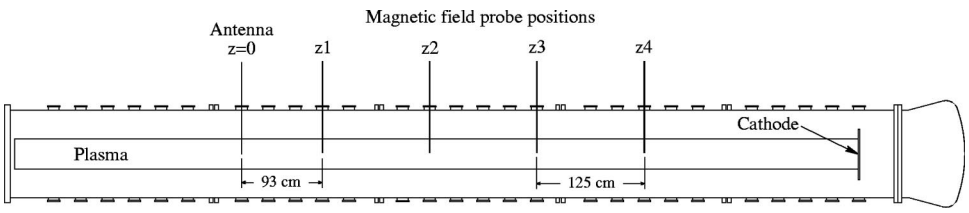

FIG. 2. Overhead view of the LaPD showing the position of the wave launching antenna (at $z=0$) and the four B-field probe measurement locations ($z=z_1,z_2,z_3,z_4$) during the uniform-background-field parallel phase velocity measurements.

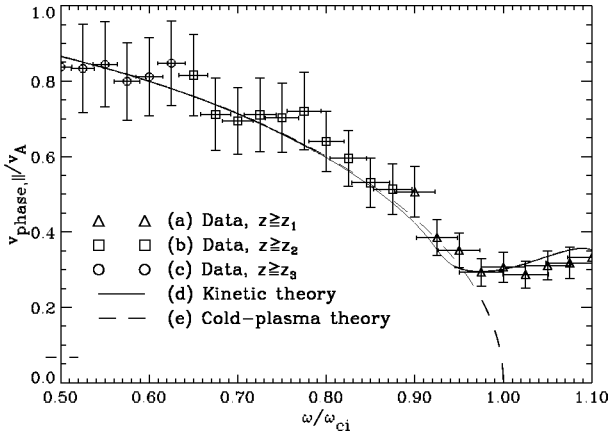

FIG. 3. Parallel phase velocities for the shear Alfvén wave in a uniform plasma. Shown are (a)–(c) measurements, (d) results from kinetic theory, and (e) results from cold-plasma theory. The measurements are all made at least one parallel wavelength from the exciter and are coded to indicate which z-locations (see Fig. 2) were used to determine the phase velocities.

peated until 25 uniformly spaced values of $\bar{\omega}$ ranging from 0.5 to 1.1 are recorded. The probe is then moved to an axial location $z_2 = 220$ cm, the $r = 0$ location is found with the same method as described above and the frequency scan is repeated. Additional frequency scans using this procedure are then performed at $z_3 = 346$ cm and $z_4 = 472$ cm. The axial spacing between successive measurement points is constant: $\Delta z = 125$ cm. The parallel phase speed of the wave is determined by measuring the delay time, Δt, between points of constant phase in the pairs of signals: (z_1, z_2), (z_2, z_3) and (z_3, z_4) for each launched frequency and computing $v_p = \Delta z / \Delta t$. In all cases, the measurement of Δt is made at times just after the active broadcast of the antenna is terminated. This is done to eliminate the possibility of signal contamination by direct pickup from the launching circuitry. Additionally, for each frequency, $\bar{\omega}$, the phase velocity determination is made using only those pairs of axial positions which both lie beyond one parallel wavelength of the antenna. This is determined by solving for $\bar{\omega}$ in the cold-plasma shear Alfvén wave dispersion relation:

$$\omega / k_\parallel = v_A \sqrt{1 - \bar{\omega}^2}, \tag{3}$$

which yields

$$\bar{\omega} = [1 + (\lambda_\parallel / 2\pi\lambda_i)^2]^{-1/2}. \tag{4}$$

Here the ion inertial length, $\lambda_i = c/\omega_{pi} = 28.7$ cm. Setting $\lambda_\parallel = z_1 = 94.3$ cm in this expression shows that the closest measurement point lies within one wavelength of the antenna for $\bar{\omega} < 0.89$. With $\lambda_\parallel = z_3 = 346$ cm, this drops to 0.46, so that the measurements of relative phase speeds between locations z_3 and z_4 are performed at an axial distance greater than one parallel wavelength from the antenna for all values of $\bar{\omega}$. Figure 3 shows the measured parallel wave phase velocity as a function of frequency. The phase velocities are normalized to the Alfvén speed and the frequencies are normalized to the ion-cyclotron frequency. The vertical error bars are due mainly to the uncertainty in Δt while the horizontal error bars are from the uncertainty in the frequency of a finite (20-cycle) tone burst. The dashed curve in Fig. 3 shows the phase velocities determined from Eq. (3) which exhibits the cold-plasma resonance at the ion-cyclotron frequency.

The solid curve shows the numerical solutions of the general dispersion relation [Eq. (2)] as computed from the experimentally measured plasma parameters and a single perpendicular wave number: $k_\perp = 0.3$ cm^{-1}; this single value was determined by selecting the dominant peak from Bessel decompositions of magnetic field profiles, $B_\theta(r)$. This peak contribution proved to be roughly invariant with respect to the wave frequency. The kinetic and cold-plasma curves both provide acceptable fits to the experimental data until approximately $\bar{\omega} = 0.95$, above which the ion kinetic effects must be included to match the observed minimum phase speed near the cyclotron frequency. Additionally, measurements of the (highly damped) shear Alfvén wave above the ion-cyclotron frequency are reproduced by the kinetic theory.

B. Nonuniform background field

1. Setup

The magnets of the LaPD are configured to produce a ''step'' magnetic field profile—with one-half of the device operating at approximately 1800 G and the other half at 900 G. A graph of the axial field profile at $r = 0$ is shown in Fig. 4; this figure also shows a drawing of the device with the same axial coordinate scaling.

With this field configuration, axial scans of the plasma are made using a Langmuir probe on opposite sides of the maximum field gradient as depicted in Fig. 4 and the results are shown in Fig. 5. The density on the low-field side of the gradient is 25% greater than on the high-field side with an average value of 2.5×10^{12} cm^{-3} and the temperature on the low-field side is approximately 10% larger than the high-field side (6.3 eV vs 5.7 eV). Although there are differences in both quantities on opposite sides of the field gradient, they appear to be localized near the region of maximum gradient $z \approx 157$ cm (relative to the antenna, located at $z = 0$). Axial measurements on the high-field side between $z = 110$ cm and $z = 140$ cm show both density and electron temperature to be nearly constant, while on the low-field side of the gradient, between $z = 175$ cm and $z = 205$ cm, the values of density and temperature are again nearly flat in this region, but with different values. In order to have some model for the complete axial variation of density and temperature, which will be needed later, we assume that in the range 0 cm$< z <$140 cm the values are constant and equal to those measured between 110 cm$< z <$140 cm, and from 175 cm$< z <$300 cm, the values are constant and equal to the measurements from 175 cm$< z <$205 cm. To model the discontinuity between these regions, which cannot be measured due to physical constraints of the experimental device, we choose to join the two regions with a linear ramp. The resulting axial profiles of density and electron temperature are also shown in Fig. 5. Finally, the low-field side plasma potential is measured to be greater by 2.2 V in the bulk of the plasma than on the high-field side, indicating an ambipolar electric field of magnitude

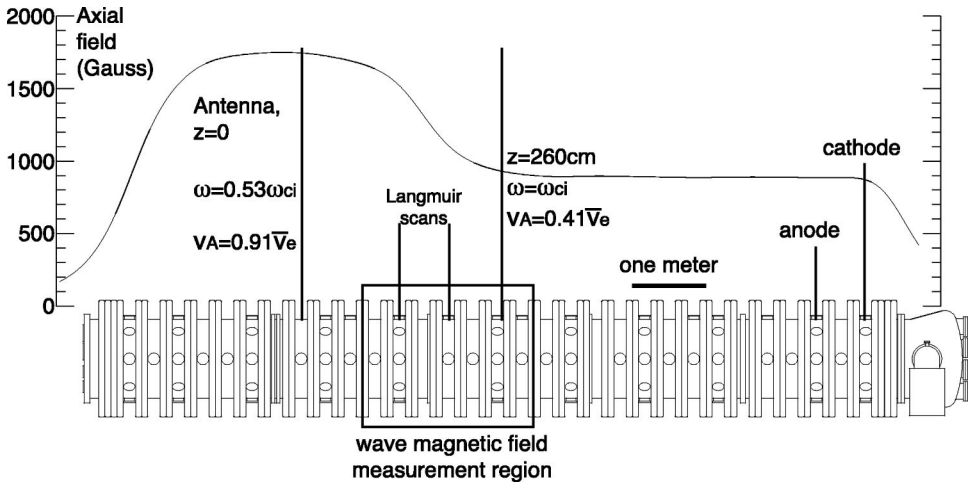

FIG. 4. Side view of the LaPD showing the magnitude of the axial magnetic field profile (at $r=0$) for the parallel-gradient magnetic field experiments. Also indicated is the region in which detailed measurements were obtained.

35 mV/cm within the gradient. As a summary of the above results a selection of plasma parameters and quantities derived from them is presented in Table I.

2. Wave launching and measurement

A disk antenna is placed at the radial center of the cylindrical plasma column at the axial location defined to be $z=0$ as depicted in Fig. 6. At this position, the launching frequency is approximately one-half of the local cyclotron frequency ($\bar{\omega}=0.53$). A tone burst of 10 cycles is launched from a positively-biased disk antenna. A plot of the modulated antenna current is shown in Fig. 7. The lower axis of this figure (τ) shows the timing of the wave experiment in units of wave periods from the beginning of the antenna current modulation. The frequency, $f=355$ kHz, is chosen so that the point $\bar{\omega}=1$ lies well within the measurement region. A tone burst (rather than a continuous wave) is employed to investigate the possibility of wave reflection from the field gradient and the ends of the device. The first and last two cycles of the input signal are attenuated with a one-quarter period sine envelope to reduce both dB/dt noise and harmonic generation at the source.

Ensemble averages (over 20 plasma discharges) of the time series of magnetic field data are acquired at six radial access ports using a triaxial magnetic induction probe. At each port, the probe samples an xz-cross-section of the plasma column. Figure 6 is an overhead view of the LaPD showing each spatial location visited during the data run by the probe. The cross-sections (xz-planes) are shown to scale within the LaPD and also enlarged for easier viewing. The number of spatial locations in each plane is not constant, but varies between 372 and 561 points. The maximum parallel field gradient occurs at $z=157$ cm, where there is no available radial access port, due to a vacuum chamber seam.

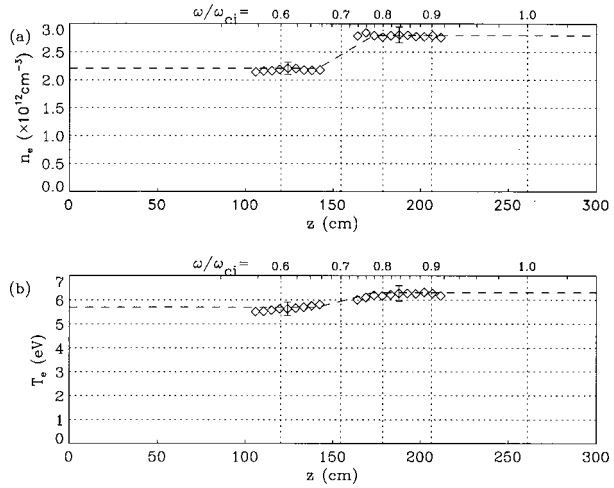

FIG. 5. Experimental electron (a) density and (b) temperature data points and extrapolated axial profiles covering the range from the antenna ($z=0$) to the farthest wave field measurement point, $z=300$ cm. The models are created from measurements in two regions: (110 cm$<z<$140 cm) and (175$<z<$205 cm) where the density and temperature are approximately flat. Since it is not mechanically possible to make measurements between $z=140$ cm and $z=175$ cm, a linear ramp is chosen to join the two regions.

3. Wave magnetic field morphology

The magnetic field data acquired on the spatial grid shown in Fig. 6 may be visualized by creating two-dimensional images of the data planes, with the shading of the images proportional to the strength of the magnetic field. Figure 8 shows how the data planes would look if the measured field were zero everywhere—all points in the image

TABLE I. Measured parameters and derived quantities at the locations of the antenna ($z=0$ cm) and the ion-cyclotron resonance point ($z=260$ cm).

Parameter	Symbol	Value at $z=0$ cm	Value at $z=260$ cm
Axial magnetic field (Gauss)	B_0	1744	926
Electron density ($\times 10^{12}$ cm^{-3})	n_e	2.2	2.8
Electron temperature (eV)	T_e	5.7	6.3
Alfvén speed ($\times 10^8$ cm/s)	v_A	1.3	0.61
Electron thermal speed ($\times 10^8$ cm/s)	$\bar{v}_e$	1.4	1.5
Ratio of wave frequency to ion-cyclotron frequency	$\bar{\omega}$	0.53	1.0
Ratio of collision frequency to angular wave frequency	Γ	1.60	1.75
Electron skin-depth (cm)	δ	0.36	0.32
Ion gyroradius (cm)	ρ_i	0.12	0.22
Ion sound-gyroradius (cm)	ρ_s	0.28	0.55

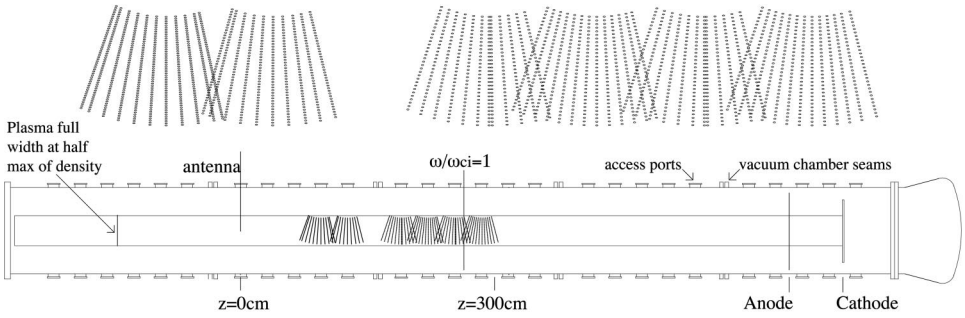

FIG. 6. Overhead view of the LaPD for the parallel gradient magnetic field experiments. Each spatial location visited by the magnetic field probe during the experiment is marked with a dot within the device and in an enlarged view above. All spatial locations lie in the plane $y=0$, in which $B_y = \mathrm{sgn}(x)B_\theta$. The arc-like shape of the data planes is a consequence of the motion of the probe.

have the same green color. This view also shows various elements of the experimental setup which, to reduce clutter, are not present in subsequent figures.

The instantaneous spatial patterns of the *y*- and *z*-components of the wave are displayed as color images in Fig. 9 for the time $\tau=5$. This time is at the middle of the antenna modulation and well into an observed CW-pattern of the fields. The radiated magnetic field is primarily B_θ, so that B_y changes sign about $x=0$. The phase fronts of the wave are identifiable as continuous color regions (either red or blue), and zero field as green. The *r*-component of the wave field is not discernible from the combination of background noise and probe misalignments. The maximum instantaneous absolute value of B_y at this time is approximately equal to 40 mG—notice that the colorbar values for B_y in this figure extend from -20 mG to $+20$ mG. This half-max scaling emphasizes phase front information rather than the precise location of wave-field extrema. Figure 9 conveys a sense of the general wave behavior, namely, the following.

(1) During the active broadcast of the antenna, the wave is observed on both sides of the maximum field gradient ($z=156$ cm) but does not exist significantly beyond the location where the wave frequency matches the local ion-cyclotron frequency ($\bar{\omega}=1$ at $z=261$ cm).
(2) On the incident side of the field gradient, the wave is almost entirely B_θ, with B_z only significantly noticeable on the low-field side of the gradient in the region $0.8 \lesssim \bar{\omega} \lesssim 1.0$.

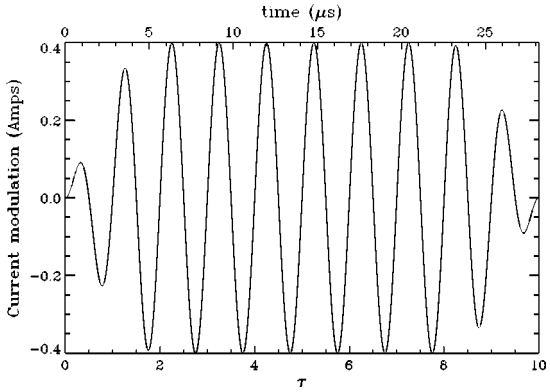

FIG. 7. Modulated current signal to the antenna shown as a function of absolute time (in micro-seconds) and as the time in wave periods since the beginning of the pulse: τ.

(3) The parallel wavelength decreases with increasing $\bar{\omega}$, reaching a minimum but nonzero value at $\bar{\omega}=1$.

One question which arises is that of wave reflection. To study this, *xz*-cross-sections of the spatial wave patterns of B_y are displayed in Fig. 10 for times before, during, and after the termination of the antenna current modulation: $\tau=(7,8,9,10,11)$; the reader may wish to refer to the input signal graph of Fig. 7. As in the previous figure, the phase fronts of the wave are identifiable as regions of either red or blue. These phase fronts propagate from left to right although the movement is not apparent in this figure since the snapshots are taken at whole-number increments of the wave period. At $\tau=7$, the wave can be seen on both sides of the maximum field gradient. The amplitude of the incident wave diminishes (as seen in the leftmost two planes) from $\tau=7$ to $\tau=10$. At $\tau=10$ and later, the phase fronts of the wave are only discernible on the low-field side of the gradient. In quantitative terms, the ratio of the maximum amplitude measured on the high-field side of the gradient at $\tau=7$ to that at $\tau=10$ is 0.04 ± 0.02. Thus there is no appreciable reflection of wave energy from the field gradient. Furthermore, since the region of a high magnetic field is approximately axially symmetric about the antenna at $z=0$ (Fig. 4), reflections of the wave from the region $z<0$ may also be ruled out.

4. WKB model and wave damping

To study damping of the wave, we first develop a WKB solution for the expected wave behavior along a ray path in the axially varying plasma. This solution is then compared with experimental data. An analysis of shear Alfvén wave propagation in an axially nonuniform plasma leads to the following differential equation for the azimuthal wave magnetic field:

$$\left(\frac{\partial^2}{\partial z^2}+k_\parallel^2-\frac{1}{\epsilon_{xx}}\frac{\partial \epsilon_{xx}}{\partial z}\frac{\partial}{\partial z}\right)B_\theta=0, \tag{5}$$

where $k_\parallel$ is the local parallel wavenumber as calculated for a uniform plasma. A WKB-type solution of Eq. (5) is sought where B_θ has the general form

$$B_\theta=A(z)\exp\left[i\int_0^z k_\parallel(z')dz'\right]. \tag{6}$$

Inserting Eq. (6) into Eq. (5) yields an approximate solution for $A(z)$:

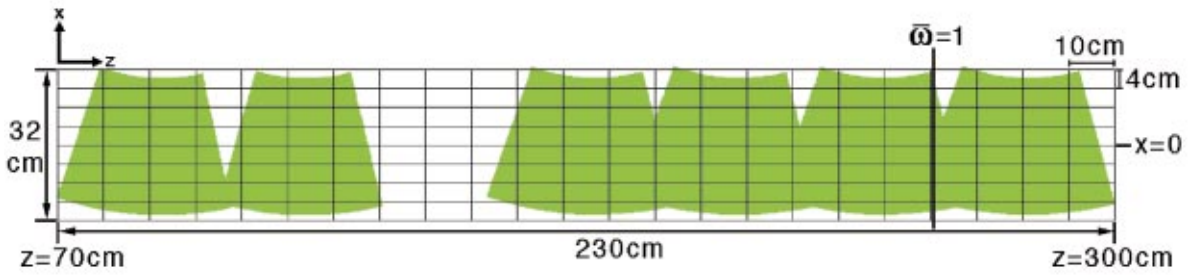

FIG. 8. (Color) Orientation figure for the images of the xz-planes.

$$A(z)=A_0\sqrt{\frac{\epsilon_{xx}}{k_\parallel}}. \tag{7}$$

To simplify the analysis and to compare with the data, the general solution is written in the following form:

$$B_\theta=A_0\sqrt{\frac{\epsilon_{xx}}{k_\parallel}}e^{-\kappa(z)}\cos[\phi(z)+\phi_0], \tag{8}$$

where

$$\phi(z)=\int_0^z \mathrm{Re}[k_\parallel(z')]dz'$$

and

$$\kappa(z)=\int_0^z \mathrm{Im}[k_\parallel(z')]dz'.$$

The initial amplitude and phase (A_0 and ϕ_0, respectively) are free parameters of the model and will be used to optimize the fit to the data. The parallel wavenumber as a function of z is numerically computed from local solutions of the dispersion relation [Eq. (2)] using the axial magnetic field profile of Fig. 4 and the continuous density and electron temperature profiles shown in Fig. 5. The only fixed quantities are the wave frequency (355 kHz) and ion temperature (1 eV). The wave damping by electrons in the theoretical model may be suppressed by setting $\Gamma=0$ in $\epsilon_\parallel$ and by using the small-argument approximation for the derivative of the plasma dispersion function: $Z'\approx-2$. With these limits, the electrons respond adiabatically to the presence of the wave fields. Additionally, collisional damping may be removed from the model while retaining electron Landau damping by making the single approximation that $\Gamma=0$.

In order to compare these WKB results with the experiment, we must interpolate the two-dimensional dataset onto a one-dimensional ray path. Figure 11 shows the y-component of the wave magnetic field in the region: $x<0$, at an arbitrary time: $\tau=5.4$. As can be seen in Fig. 6, this lower half-plane benefits from overlapping spatial data points, while the upper

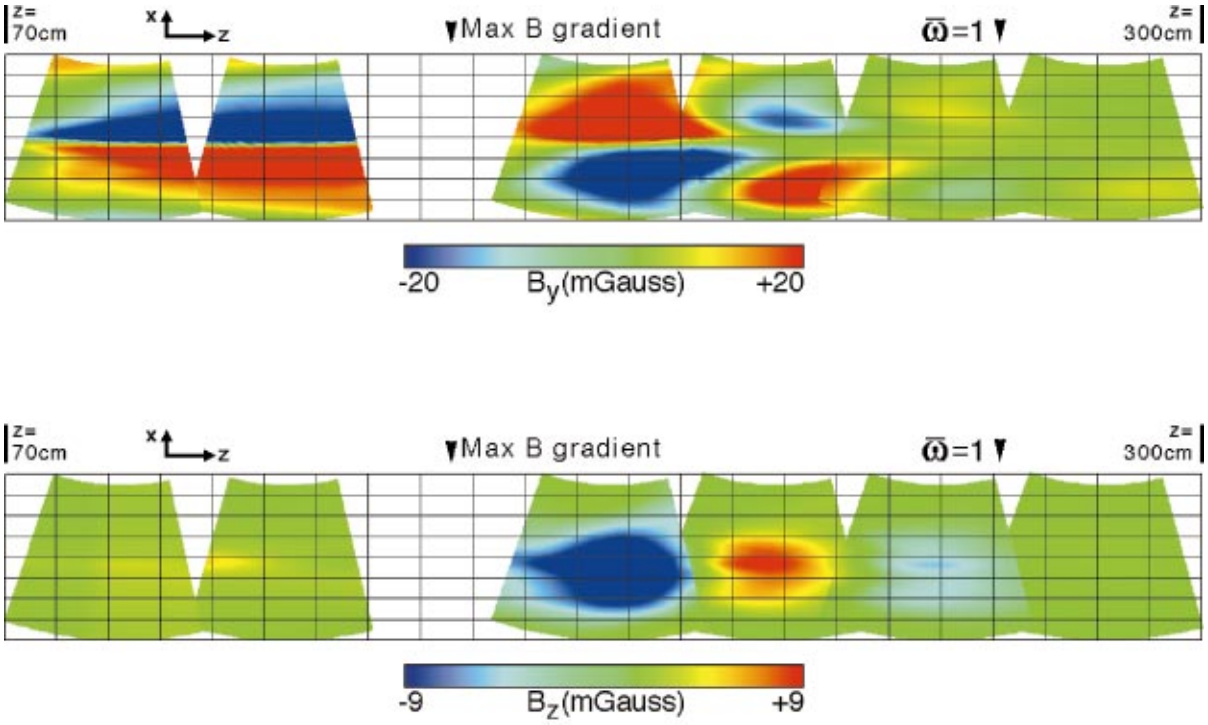

FIG. 9. (Color) Cross-sections of the instantaneous wave magnetic field B_y (top) and B_z (bottom) at $\tau=5$ in the plane $y=0$. The wave is launched from the source at $z=0$ and propagates from left to right. The maximum rms-amplitude of B_z is observed at approximately $\bar{\omega}=0.85$.

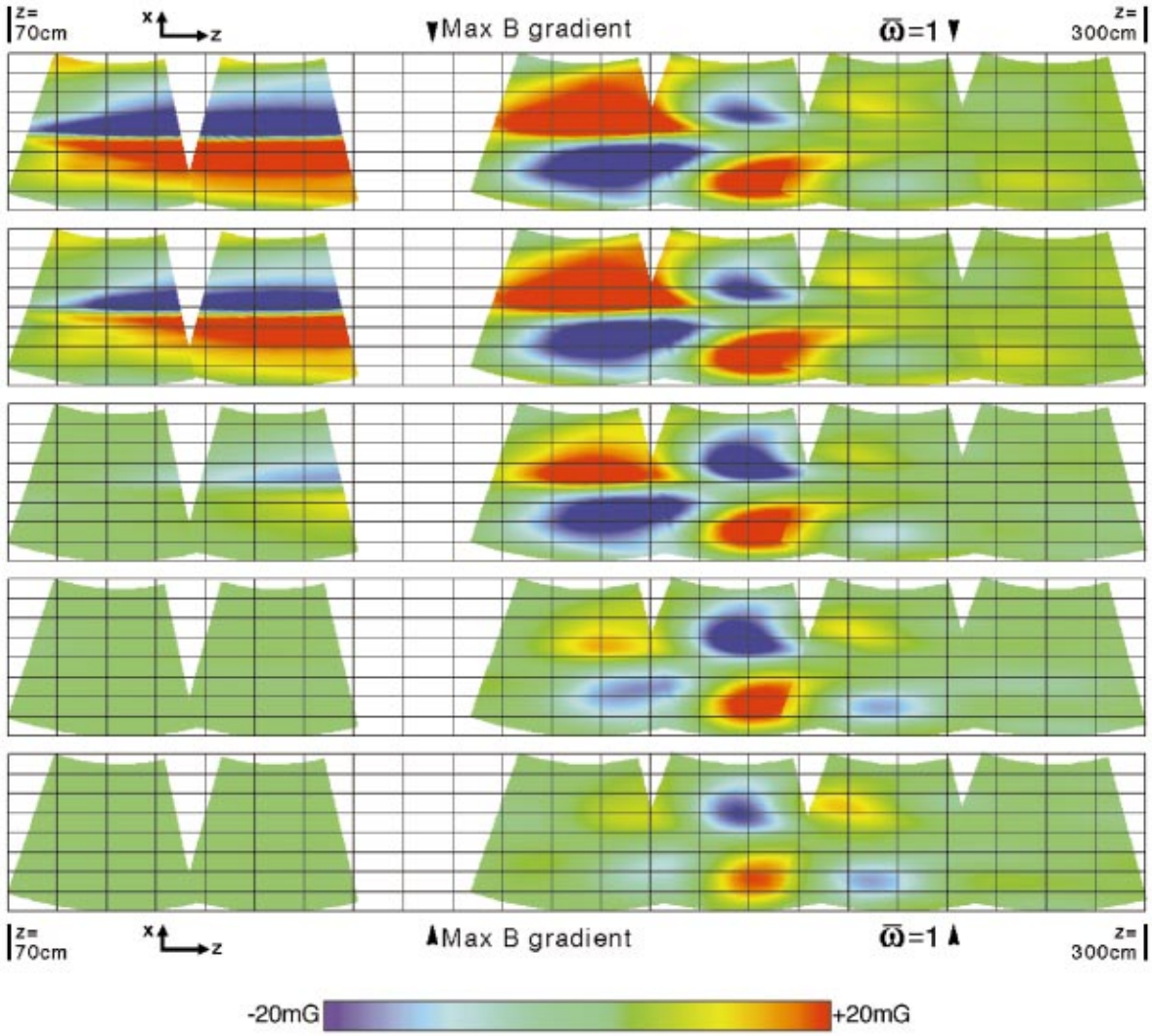

FIG. 10. (Color) Cross-sections (in the plane $y=0$) of the instantaneous wave magnetic field B_y at five different times near the end of the launched pulse: $\tau=(7,8,9,10,11)$. The topmost image is at $\tau=7$ and time increases downward. The input modulation is completely terminated by $\tau=10$. The wave propagates from left to right, and there is no noticeable evidence for a reflection of the wave from the parallel field gradient.

half plane would suffer from gaps in the data at the machine port spacing. In using only the $x<0$ data we assume that the magnetic field pattern is azimuthally symmetric, which is largely supported by Fig. 10. Also shown in Fig. 11 is a black curve representing the ray path along which the data are to be interpolated. This path is calculated by integrating the group velocities parallel,

$$v_{g,\parallel}=\frac{v_A}{1+k_\perp^2\rho_s^2}(1-\bar{\omega}^2+k_\perp^2\rho_s^2)^{3/2},$$

and perpendicular,

$$v_{g,\perp}=\frac{\omega}{k_\perp}\frac{k_\perp^2\rho_s^2}{1+k_\perp^2\rho_s^2},$$

to the local magnetic field line. Here, ρ_s is the ion sound gyroradius: $\rho_s\equiv(T_e/m_i)^{1/2}/\omega_{ci}$. Strictly speaking, the above expressions for the group velocities are valid in the kinetic limit ($v_A<\bar{v}_e$). Although the wave is launched in a region

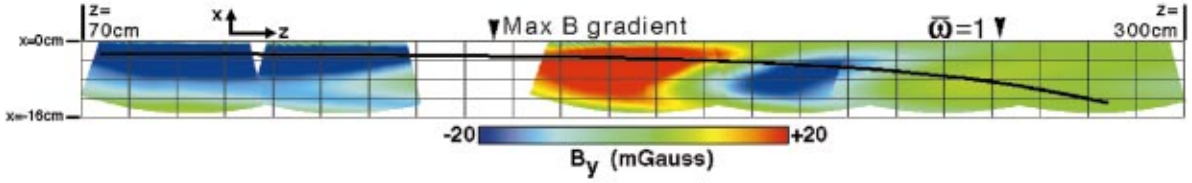

FIG. 11. (Color) Measurements of the instantaneous spatial pattern of the y-component of the wave magnetic field, B_y at time, $\tau=5.4$. The black curve indicates the ray path along which the two-dimensional data were interpolated in order to compare with the WKB results.

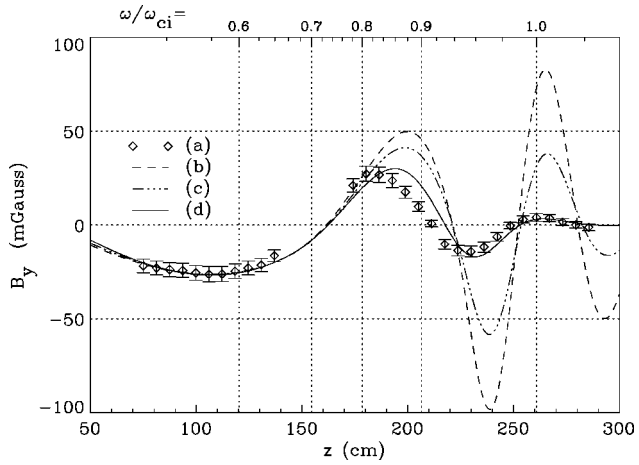

FIG. 12. A comparison of B_y axial profiles between (a) measured data points, and the WKB model of Eq. (8), with $k_\parallel$ calculated considering (b) ion-cyclotron damping only; (c) ion-cyclotron damping plus electron Landau damping; (d) the same as (c) plus electron–ion Coulomb collisions. The data are taken at time $\tau=5.4$ and interpolated along a ray path as discussed in the text and shown in Fig. 11.

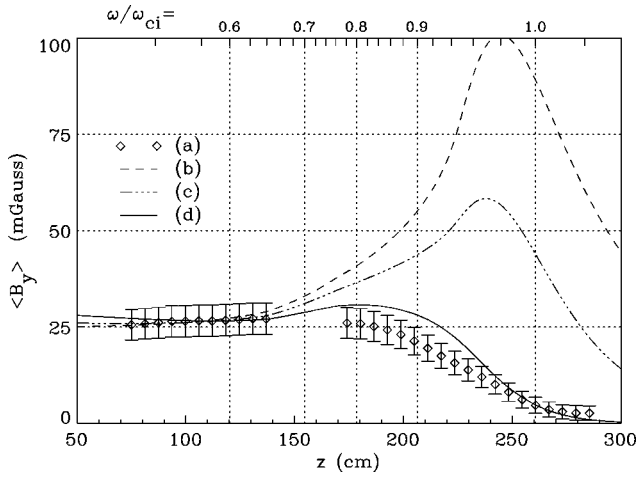

FIG. 13. Axial amplitude decay of the *y*-component of the wave magnetic field. Shown are the experimental rms amplitude data (a) compared with the WKB results which include (b) ion-cyclotron damping only; (c) ion-cyclotron damping plus electron Landau damping; (d) the same as (c) plus electron–ion Coulomb collisions. The wave amplitude is a free parameter of the model and for a comparison, the theoretical curves have been scaled by a factor which produces the best least-squares fit to the data in the region of the incident wave ($z<150$ cm).

where $v_A \approx \overline{v_e}$, in general the group velocity is nearly field-aligned ($v_{g,\parallel} \gg v_{g,\perp}$) until $\overline{\omega} \approx 1$ by which point the wave has entered the kinetic regime.

The starting point for the ray path is chosen to coincide with a peak in the rms amplitude of the incident wave magnetic field at $(r,z)=(-2.5,75)$ cm. The group velocities are calculated using a perpendicular wavenumber, $k_\perp = 0.7$ cm^{-1}. Since the azimuthal magnetic field can be expanded as a series of the Bessel functions, $J_1(k_n r)$, this corresponds to the third radial eigenmode in a 14.5 cm radius plasma column and was chosen to provide the best match between the data and the WKB model. The sensitivity of the model to the choice of $k_\perp$ will be discussed in the next section.

The comparison of the WKB model with the interpolated data is given in Fig. 12 which shows the following:

(a) Experimental data
(b) Theory with kinetic ions ($T_i=1$ eV), adiabatic electrons
(c) Theory with kinetic ions and electron Landau damping
(d) Theory with kinetic ions, electron Landau damping and electron–ion Coulomb collisions.

The initial amplitude and initial phase for all three theory plots are adjusted to match the experimental peak of the incident wave at $z \approx 110$ cm.

The phase as a function of *z* is fairly well matched by all three theoretical profiles, with the most significant deviation occurring at the point just after the wave emerges from the maximum field gradient region ($z \approx 175$ cm). Calculations using the average values for density and electron temperature throughout the measurement volume and only varying the background field strength produce plots with a phase jump roughly twice as large (compared with Fig. 12) across the maximum field gradient region. Thus, the wave field measurements are consistent with the Langmuir probe measurements which show a rapid change in electron density and temperature across the gradient.

Unlike the wave phase, fits of the axial decay in wave amplitude show significant variations depending on which damping effects are included, as shown in Fig. 13. The instantaneous phase information has been removed from the data by computing one-period rms values of the *y*-component of the wave magnetic field signal (multiplied by $\sqrt{2}$ to give the actual amplitude) centered about the time $\tau=5.4$. The data are compared with the WKB model amplitude envelope: $A(z)e^{-\kappa(z)}$ for the three damping cases as in Fig. 12 with the values of the fitting parameter, A_0 unchanged.

As was true with Fig. 12, the best theoretical fit to the amplitude data is given in Fig. 13(c) which includes the kinetic effects of ions (ion-cyclotron damping for $\overline{\omega} \approx 1$) and electrons (Landau damping and electron–ion Coulomb collisions.) All three theoretical amplitude curves show the competition between the decrease in amplitude due to energy transfer from the wave to the particles and the amplitude increase resulting from the slowing group velocity and conservation of energy. The lack of a resonant amplitude increase in the data near $\overline{\omega}=1$ emphasizes the importance of including the electron damping mechanisms. When considering ion-cyclotron damping only, the theoretically expected amplitude of the wave at $\overline{\omega}=1$ is 86 mG, yet the amplitude is 42 mG when electron Landau damping is added and only 4.3 mG (coincident with the measured value) when Coulomb collisions are also included. Thus, the actual wave amplitude is a factor of 20 times smaller at the resonance point than what would be predicted if the electrons had been ignored.

Of course, there is not a true resonance point since the ions have a finite temperature. The location of the onset of ion-cyclotron damping can be seen in Fig. 14 which shows

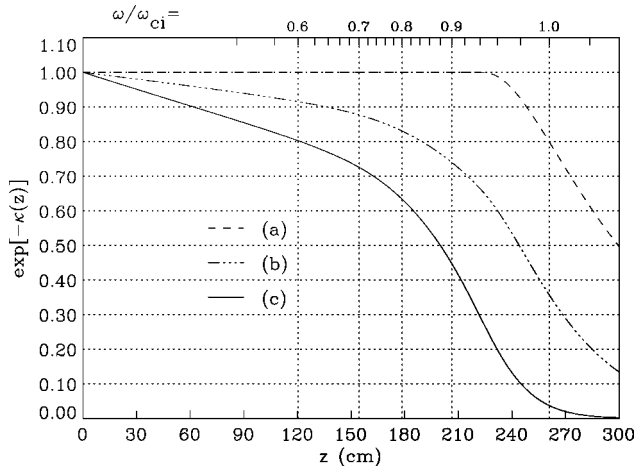

FIG. 14. Spatial behavior of the exponential damping factor: $\exp[-\kappa(z)]$. Shown are the results of the WKB model which include (a) ion-cyclotron damping only; (b) ion-cyclotron damping plus electron Landau damping; (c) the same as (b) plus electron-ion Coulomb collisions.

the theoretical decay envelopes from the WKB model: $\exp[-\kappa(z)]$. Curve (a) of Fig. 14 shows the spatial decay of the wave amplitude due to ion-cyclotron damping alone. For helium ions at 1 eV in this experiment, the resonant interaction is still limited to a fairly narrow range: $\bar{\omega} > 0.94$. However, curves (b) and (c) show a steady loss to the electrons well before this point. In addition, both electron Landau damping and electron–ion Coulomb collisions show roughly equal contributions to the axial amplitude decay.

5. Sensitivity of the model to $k_\perp$

The model results of the previous section require the selection of a single perpendicular wavenumber in order to compute both the ray path and the axial variation of the parallel wavenumber. But, what radial wavenumbers are available for making this selection and how do they affect the fit of the WKB model to the data?

Figure 15 shows fits of the model (using all three damping mechanisms) to the interpolated data for three perpendicular wavenumbers: $k_\perp = (0.48, 0.70, 0.92)$ cm^{-1}. These correspond to the 2nd, 3rd, and 4th radial eigenmodes, respectively, of the azimuthal component of the wave magnetic field. As before, the amplitudes and phases of the theoretical profiles are adjusted to match the experimental peak of the incident wave at $z \approx 110$ cm. In each case, the data were interpolated along the appropriate group velocity path. For the case $k_\perp = 0.48$ cm^{-1}, the interpolated data points do not extend axially as far as the other cases since the ray path extends beyond the radial extent of the measurement volume soon after $\bar{\omega} = 1$. Since the value $k_\perp = 0.7$ cm^{-1} was used in the previous section, this figure shows the comparison of that fit to the two nearest allowable radial wavenumbers. The chosen $k_\perp = 0.7$ cm^{-1} provides the best fit in a least-squares sense to the data. Higher wavenumbers exhibit greater damping and longer parallel wavelengths near the cyclotron resonance. The opposite is true (less damping and shorter wavelengths) for wavenumbers smaller than the chosen one.

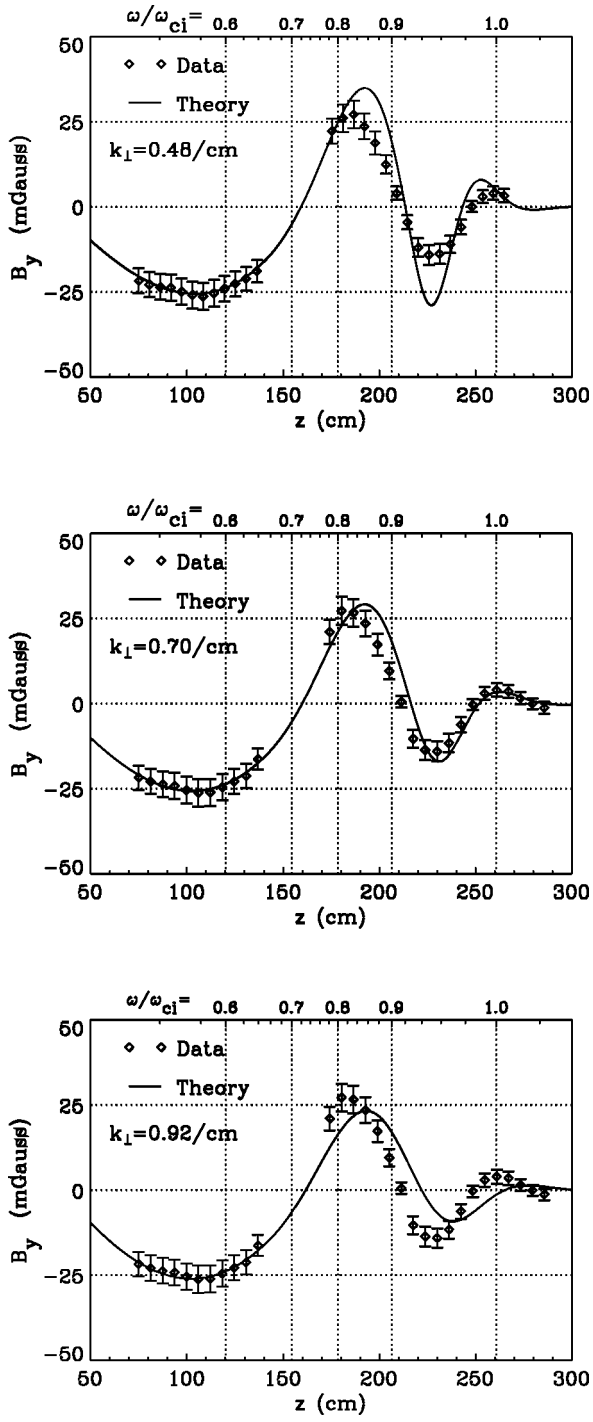

FIG. 15. A comparison of the WKB model fits for three different perpendicular wavenumbers: $k_\perp = (0.48, 0.70, 0.92)$ cm^{-1}. These correspond to the 2nd, 3rd, and 4th radial eigenmodes, respectively, of the azimuthal component of the wave magnetic field.

6. Parallel wave electric field

Since it is through the parallel electric field that the electrons take energy from the wave, it is desirable to understand the axial variation in $E_\parallel$; unfortunately, the parallel electric fields of the wave are too small to be measured with available diagnostics. However, an indirect measurement can be made as follows: neglecting the displacement current for

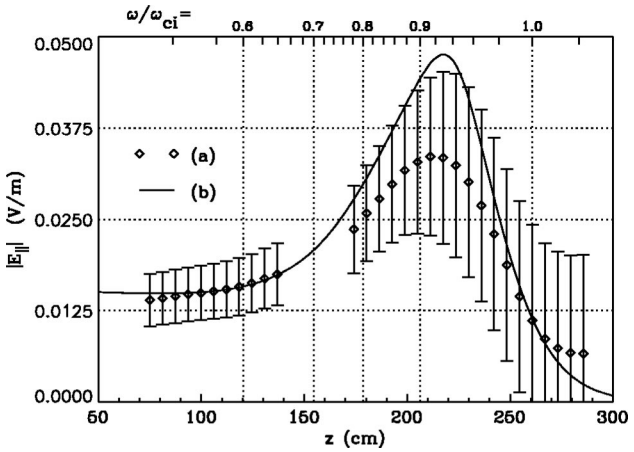

FIG. 16. Magnitudes of the parallel electric field computed from Eq. (9). Shown are (a) results derived from the measured azimuthal magnetic field amplitude, and (b) the WKB model using the amplitude from curve (d) of Fig. 13.

these low-frequency waves, the azimuthal magnetic field as a function of k may be obtained[14] using the z-component of Ampère's law:

$$B_\theta = \frac{4\pi}{ck_\perp} j_\parallel ,$$

and (with $\epsilon_\parallel - 1 \approx \epsilon_\parallel$) the current density may be written in terms of the electric field by

$$j_\parallel = \frac{\omega}{4\pi i} \epsilon_\parallel E_\parallel .$$

Then, solving for the absolute value of $E_\parallel$ in terms of B_θ, and as a function of z, we have

$$|E_\parallel(z)| = \frac{ck_\perp}{\omega} \frac{B_\theta(z)}{|\epsilon_\parallel(z)|}. \tag{9}$$

The predictions of Eq. (9) are plotted in Fig. 16 which shows two cases for the magnetic field amplitude, $B_\theta(z)$: (a) the measured rms values from Fig. 13(a), and (b) the WKB model amplitude envelope: $A(z)e^{-\kappa(z)}$ from curve (d) of Fig. 13.

Both the data and theory show three main features: first, on the incident wave side ($\bar{\omega} < 0.7$) the parallel electric field is roughly constant which implies a steady loss of wave energy to the electrons through Landau damping; second, as the parallel wavelength decreases near the ion-cyclotron frequency ($0.7 < \bar{\omega} < 0.94$) there is a region of increased electric field and, thus, increased electron dissipation; finally, above $\bar{\omega} = 0.94$ the rapid decay of the azimuthal magnetic field amplitude results in a corresponding drop in the parallel electric field. These results, of course, rely on the WKB model for the axial variation of $\epsilon_\parallel$ and not direct measurements of the parallel electric field.

V. CONCLUSIONS

We have studied the propagation and damping of a shear Alfvén wave launched by a disk antenna of skin-depth radius in a magnetic beach geometry. Disk antennas excite the wave by modulating the field-aligned electron currents drawn to them and radiate azimuthally symmetric shear waves with finite perpendicular wavelengths and parallel electric fields. Before performing experiments in a nonuniform magnetic field, the wave dispersion was measured in a uniform magnetic field for a range of frequencies from $\omega = 0.5\omega_{ci}$ to $\omega = 1.1\omega_{ci}$. Phase velocity measurements agreed with a kinetic dispersion relation over the entire frequency range.

The same antenna was then placed in a plasma with a nonuniform background magnetic field and a phase-locked toneburst was applied to the antenna such that the broadcast frequency was approximately one-half of the local ion-cyclotron frequency. In addition, the Alfvén speed at the antenna was approximately equal to the electron thermal speed. The time evolution of the radiated wave magnetic fields was measured in a series of spatial planes which sampled the wave magnetic field both parallel and perpendicular to the background field. The wave was observed to propagate into the decreasing background field to a region where the wave frequency matched the local ion-cyclotron frequency and the Alfvén speed was approximately one-half the electron thermal speed. No reflected wave was observed.

The measured axial variations of the wave amplitude and phase were well reproduced by a WKB model of an incident plane wave which propagated and damped according to local solutions of the same kinetic dispersion relation used in the uniform field experiment. The satisfactory fit to the data required the inclusion of ion-cyclotron damping, electron Landau damping, and electron-ion Coulomb collisions. By considering ion-cyclotron damping alone, the predicted wave magnetic field amplitude at the location of ion-cyclotron resonance was 20 times greater than both the measured value and the value predicted by also including electron losses.

Although the shear Alfvén wave is primarily thought of as being an ion wave, it is important to determine if there are any regions in which the electron dynamics must be considered. Failure to do so can result, for example, in an incomplete assessment of the efficiency of laboratory ion-cyclotron heating experiments which rely on the placement of antennas in cold, rarefied edge plasmas. In fact, the wave may modify the electron distribution function which could result in unwanted plasma perturbations. Furthermore, as pointed out by Streltsov and Lotko,[15] wave–electron interactions may play an important role in understanding the dynamics of resonances in the Earth's magnetosphere where standing Alfvén waves along auroral magnetic field lines may continually make the transition between the kinetic and inertial regimes as they propagate through the magnetospheric plasma and are reflected between ionospheric endpoints.

ACKNOWLEDGMENTS

The authors wish to thank Professor George Morales and Dr. David Leneman for their valuable discussions and contributions.

This work was funded by ONR Grant No. N00014-97-1-0167, NSF Grant No. ATM-970-3831, and DOE Grant No. DE-FG03-00ER54598.

[1]T. H. Stix and R. W. Palladino, in *Proceedings of the 2nd UN International Conference on the Peaceful Uses of Atomic Energy*, Geneva, 1958, No. 31, p. 282.
[2]F. I. Bowley, J. M. Wilcox, A. W. DeSilva, and P. R. Forman, Phys. Fluids **6**, 925 (1963).
[3]Y. Amagishi, A. Tsushima, and M. Inutake, Phys. Rev. Lett. **48**, 1183 (1982).
[4]L. C. Woods, J. Fluid Mech. **13**, 570 (1962).
[5]D. G. Swanson, R. W. Clark, P. Korn, S. Robertson, and C. B. Wharton, Phys. Rev. Lett. **28**, 1015 (1972).
[6]R. A. Breun, P. Brooker, D. Brouchous, J. Browning, G. Butz, J. Conrad, E. Dales, J. Ferron, R. Goulding, N. Hershkowitz, T. Intrator, C. Litwin, R. Majeski, S. Maessick, B. Nelson, L. Peranich, H. Persing, J. Radtke, D. Roberts, G. Severn, D. Sing, E. Wang, D. A. D'Ippolito, J. R. Myra, and G. L. Francis, in *11th IAEA International Conference on Plasma Physics and Controlled Nuclear Fusion Research*, Kyoto, Japan, 13–20 November 1986, Vol. 2 of Nuclear Fusion Supplement, 1987, pp. 263–271.
[7]Y. Yasaka, R. Majeski, J. Browning, N. Hershkowitz, and D. Roberts, Nucl. Fusion **28**, 1765 (1988).
[8]D. R. Roberts, N. Hershkowitz, R. P. Majeski, and D. H. Edgell, in *8th Topical Conference on Radio-Frequency Power in Plasmas*, Vol. 190 of AIP Conference Proceedings (American Institute of Physics, NY, 1989), pp. 462–465.
[9]A. V. Zvonkov and A. V. Timofeev, Sov. J. Plasma Phys. **13**, 158 (1987).
[10]S. J. Zweben, C. R. Menyuk, and R. J. Taylor, Phys. Rev. Lett. **42**, 1270 (1979).
[11]G. G. Borg, M. H. Brennan, R. C. Cross, L. Giannone, and I. J. Donnelly, Plasma Phys. Controlled Fusion **27**, 1125 (1985).
[12]R. C. Cross, B. W. James, H. C. Kirbie, J. A. Lehane, and S. W. Simpson, At. Energ. **24**, a221 (1982).
[13]G. J. Morales, R. S. Loritsch, and J. E. Maggs, Phys. Plasmas **1**, 3765 (1994).
[14]G. J. Morales and J. E. Maggs, Phys. Plasmas **4**, 4118 (1997).
[15]A. Streltsov and W. Lotko, J. Geophys. Res. **100**, 19457 (1995).
[16]W. Gekelman, D. Leneman, J. Maggs, and S. Vincena, Phys. Plasmas **1**, 3775 (1994).
[17]W. Gekelman, S. Vincena, D. Leneman, and J. Maggs, J. Geophys. Res. **102**, 7225 (1997).
[18]D. Leneman, W. Gekelman, and J. Maggs, Phys. Plasmas **7**, 3934 (2000).
[19]S. T. Vincena and W. N. Gekelman, IEEE Trans. Plasma Sci. **27**, 144 (1999).
[20]D. A. Gurnett and L. A. Frank, J. Geophys. Res. **77**, 3411 (1972).
[21]M. Temerin and R. L. Lysak, J. Geophys. Res. **89**, 2849 (1984).
[22]H. Saito, T. Yoshino, and N. Sato, Planet. Space Sci. **35**, 745 (1987).
[23]G. Gustafsson, M. Andre, L. Matson, and H. Koskinen, J. Geophys. Res. **95**, 5889 (1990).
[24]P. Louarn, J. E. Wahlund, T. Chust, H. de Feraudy, A. Roux, B. Holback, P. O. Dovner, A. I. Eriksson, and G. Holmgren, Geophys. Res. Lett. **21**, 1847 (1994).
[25]M. Volwerk, P. Louarn, T. Chust, A. Roux, H. de Feraudy, and B. Holback, J. Geophys. Res. **101**, 13335 (1996).
[26]C. W. Carlson, R. F. Pfaff, and J. G. Watzin, Geophys. Res. Lett. **25**, 2013 (1998).
[27]J. P. McFadden, C. W. Carlson, R. E. Ergun, C. C. Chaston, F. S. Mozer, M. Temerin, D. M. Klumpar, E. G. Shelley, W. K. Peterson, E. Möbius, L. Kistler, R. Elphic, R. Strangeway, C. Cattell, and R. Pfaff, Geophys. Res. Lett. **25**, 2045 (1998).
[28]E. J. Lund, E. Möbius, L. Tang, L. M. Kistler, M. A. Popecki, D. M. Klumpar, W. K. Peterson, E. G. Shelley, B. Klecker, D. Hovestadt, M. Temerin, R. E. Ergun, J. P. McFadden, C. W. Carlson, F. S. Mozer, R. C. Elphic, R. J. Strangeway, C. A. Cattell, and R. F. Pfaff, Geophys. Res. Lett. **25**, 2049 (1998).
[29]W. Gekelman, J. Geophys. Res. **104**, 14417 (1999).
[30]T. H. Stix, *Waves in Plasmas* (McGraw-Hill, New York, 1992).
[31]B. D. Fried and S. D. Conte, *The Plasma Dispersion Function* (Academic, New York, 1961).
[32]G. P. M. Poppe and C. M. J. Wijers, ACM Trans. Math. Softw. **16**, 38 (1990).
[33]R. A. Koch and W. Horton, Jr., Phys. Fluids **18**, 861 (1975).
[34]W. Gekelman, H. Pfister, Z. Lucky, J. Bamber, D. Leneman, and J. Maggs, Rev. Sci. Instrum. **62**, 2875 (1991).
[35]M. A. Gilmore, Ph.D. thesis, University of California at Los Angeles, 1999.
[36]L. Mandrake and W. Gekelman, Comput. Phys. **11**, 498 (1997).